Three-Dimensional Imaging of Large Compressive Deformations in Elastomeric Foams

J. H. KINNEY,[1] G. W. MARSHALL,[1] S. J. MARSHALL,[1] D. L. HAUPT[2]

[1] Department of Restorative Dentistry, University of California San Francisco, San Francisco, California 94143

[2] Department of Mechanical Engineering, Lawrence Livermore National Laboratory, Livermore, California 94551

ABSTRACT: Specimens of silica-reinforced polysiloxane foam pads were three-dimensionally imaged during axial compressive loading to densification. The foams' behavior was highly nonlinear and showed the three characteristic regions of linear elastic, elastic buckling, and densification. A finite-element technique, based upon conversion of the image voxels to finite elements, was used to calculate the mechanical properties of the foams. The results were compared with conventional mechanical testing and theory. The finite-element calculations were in excellent agreement with experimental stress–strain data over the entire range of compressive loading. Theoretical models, on the other hand, overestimated the stiffness of the foam above the elastic buckling stress by not correctly predicting the abruptness of the transition from elastic buckling to densification. Three-dimensional analysis of the deformed microstructures indicated that there was a critical foam density beyond which the cell morphology suddenly changed from open-celled to closed-celled and that this "phase"-like transition was responsible for the abrupt increase in stiffness near densification. © 2001 John Wiley & Sons, Inc. J Appl Polym Sci 80: 1746–1755, 2001

Key words: mechanical properties; foam; microtomography; finite-element modeling; elastomer; percolation theory

INTRODUCTION

There are many commercial uses for engineered foams. Engineered foams have been applied in sandwich panels and are frequently used in packaging and for thermal insulation. Foams are also being studied for use as porous scaffolds for tissue regeneration, particularly for cartilage and bone. The importance of these materials is reflected by the considerable literature on both their synthesis and their physical properties.[1,2]

Low-density foams have characteristic stress–strain curves when loaded in compression. A representative engineering compression curve for an elastomeric foam is shown in Figure 1. There are three distinct regions in this profile: a linear elastic region (labeled I in the inset), a postbuckling plateau region (II), and a densification region marked by a rapid rise in the stress with continued compression (III). The transition from linear to nonlinear behavior occurs at a strain (ε_{el}) associated with elastic buckling of the cell members. The transition to densification occurs at a strain (ε_D) where most of the porosity has been squeezed out and solid behavior becomes dominant.

Theoretical expressions that predict the initial linear elastic behavior of specific cellular microstructures have been derived.[3,4] All these expressions have a power-law scaling of the elastic mod-
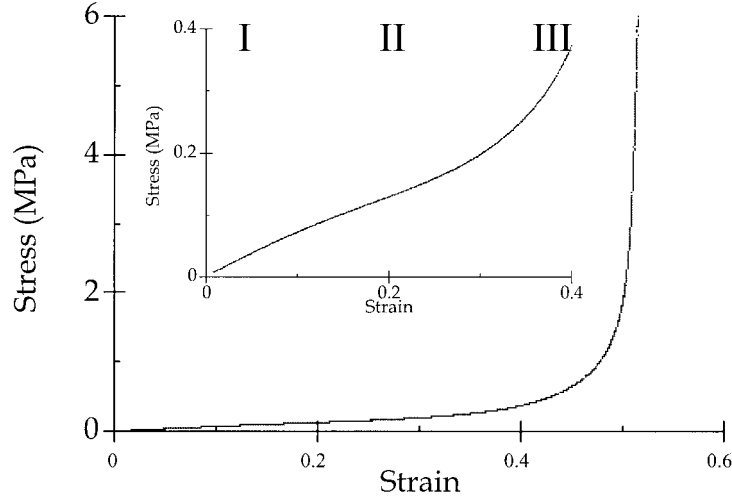
Figure 1 A representative engineering stress–strain curve for the silicone elastomeric foam imaged in this study. The initial foam density was 50%. Three regions characteristic of elastomeric foam behavior are labeled (I) linear elastic, (II) elastic buckling, and (III) densification.

ulus with foam density similar to those derived earlier by Gibson and Ashby from more idealized models of a foam's characteristic unit cell.[5] Adopting the notation of Gibson and Ashby, the elastic modulus of a closed-cell foam in the linear elastic regime is given by

$$\frac{E^*}{E_s} = \varphi^2\left(\frac{\rho^*}{\rho_s}\right)^2 + (1-\varphi)\left(\frac{\rho^*}{\rho_s}\right) + \frac{p_0(1-2\nu^*)}{E_s(1-\rho^*/\rho)_s} \quad (1)$$

In this expression, E^* and ρ^* are the modulus and the density of the foam, and the s-subscripted variables represent those same values for the solid elastomer. Also, Poisson's ratio of the foam is given by ν^*, and the fraction of solid contained in the cell edges and the cell faces are ϕ and $1-\phi$, respectively. The third term on the right-hand side of eq. (1) represents the contribution of trapped gas or liquid (filling) in the cells at an ambient pressure p_o. In an open-celled foam, this contribution is zero.

Gibson and Ashby derived the stress at which elastic collapse occurs in terms of the critical stress required for Euler buckling. This stress also follows power-law scaling and for closed-cell elastomeric foams is given by

$$\frac{\Sigma_{el}}{E_s} \cong .03\left(\frac{\rho^*}{\rho_s}\right)^2\left(1+\left(\frac{\rho^*}{\rho_s}\right)^{1/2}\right)^2 + \frac{(p_0-p_{at})}{E_s} \quad (2)$$

In the above expression, p_{at} is the atmospheric pressure; if the ambient cell pressure and atmo-

spheric pressure are equal, then the pressure-dependent term vanishes. The leading coefficient was derived from fitting the elastic collapse stress for elastomeric foams with a wide range of density.

The postbuckling curve for strains lying between ε_{el} and ε_D is more difficult to describe analytically. For open-cell foams, it is frequently found that the plateau stress remains constant with increasing strain. Closed-cell elastomers, on the other hand, often exhibit a rising, postbuckling slope. This increase is believed to result from both compression of the gas or liquid trapped within the cells and from membrane stresses.[1]

The theoretical treatment of the postbuckling behavior near densification has been problematic. BenDor et al.,[6] in their criticism of the semiemperical treatment by Gibson and Ashby, proposed a well-tailored compressive stress–strain relation for $\varepsilon > \varepsilon_{el}$:

$$\frac{\sigma}{\Sigma_{el}} = \frac{\varepsilon_D}{\varepsilon_D + \varepsilon_{el} - \varepsilon} \quad (3)$$

In the above equation, ε_D is the Gibson and Ashby estimate: $\varepsilon_D = 1 - 1.4(\rho^*/\varepsilon_s)$. Although this relationship has the advantage of avoiding the singularity when $\varepsilon = \varepsilon_D$, it is still based on emperical fits to a limited database for values of ε_D, Σ_{el}, and ε_{el}.

Recently, Dienes and Solem[7] derived an *ab initio* theory of the stress–strain relation for open-

celled elastomeric foams with spherical porosity. For materials where the bulk modulus is much greater than is the shear modulus, these investigators derived an analytical expression for post-buckling stress–strain behavior in terms of the pore fraction $V\nu$ and the shear modulus of the base elastomer, μ_s:

$$\sigma = \frac{4}{3} \frac{\mu_s \varepsilon (1 - V_\nu)^\alpha}{V\nu - \varepsilon} + \Sigma_{\text{el}} \qquad (4)$$

Here, α is given by

$$\alpha = \frac{15(1 - \nu_s)}{7 - 5\nu_s} \qquad (5)$$

Although similar in form to that proposed by Ben-Dor et al., this expression has the unique advantage that its behavior depends only on known constituent properties and the measurable pore fraction.

Our understanding of large deformation behavior in elastomeric foams should benefit from an ability to fully characterize the microstructure during loading. The present study describes a noninvasive method of imaging the architecture of cellular solids in three dimensions. By way of demonstrating the method, elastomeric foams were imaged during axial compression from the unloaded state to the beginning of densification. Attention was paid to the topology of the elastomer network and the enclosed porosity. The physical structure was meshed, and the elastic properties were calculated by the finite-element technique. The finite-element results were then compared with experimental measurements and theoretical models in the postbuckling regime. Particular emphasis was placed on the transition to densification.

EXPERIMENTAL

Materials Preparation and Imaging

Commercially available elastomer foam was used for this study. The base material was peroxide-cured polysiloxane in which ~25 wt % fumed-type silica fillers were incorporated for reinforcement. The elastic properties of the base elastomer are listed in Table I. Porosity of the foam was controlled by the use of a sacrificial pore former, or porogen, which consisted of ~0.5-mm-diameter

Table I   Initial Properties of the Foam Specimens

Specimen	Apparent Density	E_s (MPa)	ν_s	τ (μm)
9750	0.497	1.90	0.49	106
9760	0.406	1.90	0.49	77

The apparent density is the foam density as a fraction of the density of the solid elastomer. E_s and ν_s are the Young's modulus and Poisson's ratio of the solid elastomer, while τ is the average thickness of the cell walls in the foam. The values of the apparent density and the cell wall thickness were obtained from the analysis of the three-dimensional tomograms. The Young's modulus and Poisson's ratio were determined from independent measurements on the solid elastomer.

spherical urea beads. Cylindrical specimens, 15 mm in diameter, were prepared from 1-mm-thick foam pads with two initial densities: 40 and 50%.

The specimens were placed in a displacement-controlled load frame and imaged with monochromatic synchrotron radiation. Repeated images were acquired as the specimens were uniaxially compressed in stages at 0, 15, 30, and 35% strain. One complete load/unload cycle was imaged for each foam pad. The X-ray energy was 25 keV, and the rotational increment of the tomographic scanner was 0.5°.

The load stage developed for this study is shown in Figure 2. The compressive load was transferred to the specimen using a micrometer. The loading micrometer had a 0.002-mm resolution and a large pitch diameter that resulted in a low helix angle and high leverage. The bottom specimen platen was driven by the rotary stage, while the upper end of the specimen rotated on miniature precision bearings housed within an upper anvil. A main thrust bearing inside the upper anvil took the entire load of the micrometer. In addition, there were two purely radial bearings that served to ensure concentric rotation. Six, ultrafine, adjusting screws controlled the alignment of the micrometer axis with the lower rotational axis. A precision dial test indicator was used to determine coaxiality. Specimens were held between two acrylic platens that were clamped to the aluminum upper and lower anvils by three equally spaced screws.

Three-dimensional images of the deformed elastomer foams were obtained by Fourier-filtered back projection of the synchrotron data.[8] Although the ultimate spatial resolution of the scanner is 2 μm for small specimens, the large specimen diameters used in this study required
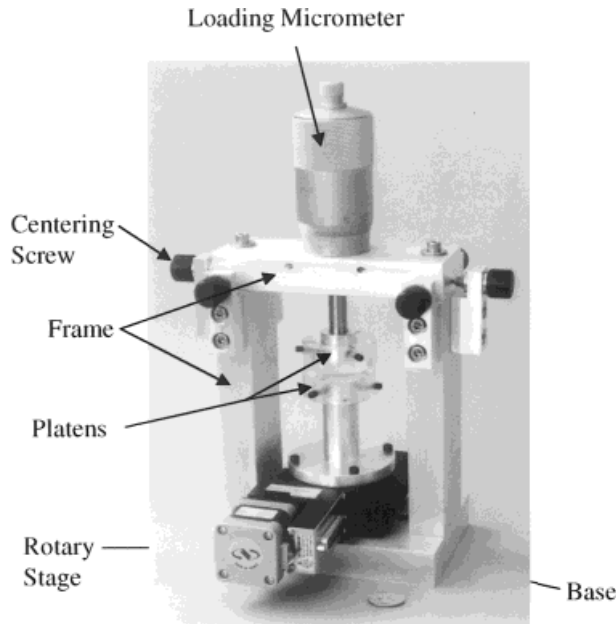
Figure 2   The loading micrometer cell used to compress the foams while performing tomographic imaging. Specimens were placed between the load platens, and compressive strains were applied by rotation of the calibrated micrometer dial.

the volume elements in the reconstructed images to be 16 μm on edge. The time required to make a complete three-dimensional image and increment the strain was just under 15 min. Imaging a complete load and recovery cycle required about 2 h of synchrotron beam time.

Characterization

Once reconstructed, the volume fraction of porosity, V_v, was determined at each stage of compression. An apparent density was defined as $\rho_a = (1 - V_v)$. A polygonal mesh, fit to the surface of the elastomer, was used to measure the surface area, S, of the elastomer. The mean cell wall thickness, τ, was calculated from the relationship between the surface and the volume ($\tau, = 2V_v/S$).[9]

There are two types of porosity in a cellular material. There are open pores that connect with the exterior of the specimen and blind pores that are sealed off from the exterior. For compressive loading, where solid platens seal off the top and bottom surfaces of the specimen, open pores were defined as those that were continuously connected with the perimeter boundary of the specimen. All other pores were defined as blind pores. An efficient connected components labeling algorithm was used to identify and label all the pores

in the foam.[10] The fraction of all pores that were connected with the perimeter surface (open porosity), X_A, was measured at each increment of compressive loading.

The connectivity of the elastomer was derived from the Euler characteristic of the specimen, X_E. The Euler characteristic was measured by Feldkamp's algorithm.[11] The connectivity, defined as the number of handles or loops in the object, was calculated for the foams by

$$\beta_1 = 1 - X_E + \beta_2 \qquad (6)$$

Here, β_1 was the connectivity, and β_2, the number of blind pores trapped within the foam.[12] The connectivity was measured before and after a full cycle of load and recovery.

Finite-element Modeling

The three-dimensional images of the cellular foams were composed of cubic volume elements that contained either an elastomer or air. It was natural to use this partitioning as the basis for finite-element modeling; each image volume element was turned into a finite element.[13] This had the advantage of nearly instantaneous implementation in going from the structural image to its finite-element representation. However, it had the disadvantage of not being an optimal meshing strategy. Each image produced the order of 10^8 finite elements. Where this method was used before, it has produced excellent agreement with experimental measurements.[14–16]

For the present study, the constituent base elastomer was modeled as an isotropic linear elastic material. The Young's modulus, E_s, and bulk modulus, k_s, were obtained from experimental measurements on the base elastomer. The three-dimensional image at zero strain was used to calculate the initial modulus of the foam E^* ($\varepsilon = 0$). The surface elements were initially displaced by 10^{-6}, and the structure was relaxed. The surface elements were laterally constrained to simulate the fixed-grip conditions at the platen–specimen boundary. This perturbation approach was then repeated with each image to obtain E^* ($\varepsilon > 0$). The calculated values of E^* were compared with the derivative of the stress–strain curve.

RESULTS

A tomographic image through the midplane of an unloaded foam is shown in Figure 3. Although the
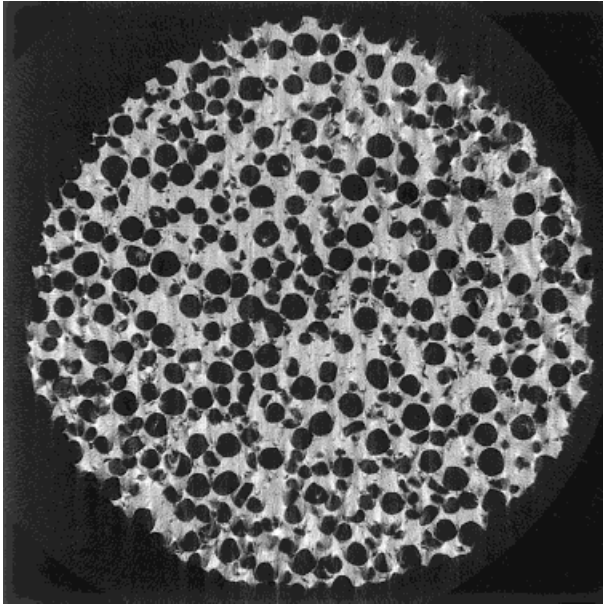
Figure 3 A tomographic cross section through the midplane of an unstrained foam specimen. The initial foam density was 50%. Although the majority of the pores were spherical, several nonspherical pores could be identified. These defective pores were believed to have been caused by fragmentation of the urea beads during mixing of the elastomer.

majority of the pores had a circular cross section, there were numerous pores with irregular shapes. These irregular pores most likely had their origins in the fragmentation of urea beads during mixing. A three-dimensional image of a 1-mm-diameter core through the specimen, shown in Figure 4, indicates that the pores were approximately spherical with circular wall openings connecting adjoining cells. No clear distinction could be made between cell edges of faces, and it was impossible to determine ϕ from the images.

Through-thickness tomographic cross sections in Figure 5 show the pore deformation during axial compression of a 50% dense foam to a 35% engineering strain. Complex patterns of cell wall buckling and folding were apparent in the images. The leftmost third of each section is shown in greater detail in Figure 6 at 0 and 15% engineering strain during both the load (left) and unload (right) cycle. The registration between the corresponding left and right images was nearly perfect, even at the smallest detail.

The open-pore fraction, X_A, is graphed as a function of the apparent density of the compressed foam in Figure 7. Initially, all the pores were open to the surface. The pores remained

Figure 4 A three-dimensional rendering of a 1-mm-diameter cylinder through the center of the foam shown in Figure 3 Circular openings connect adjacent pores.

open for most of the compression cycle. The 40% dense foam specimen, which was compressed to a 40% engineering strain, never exceeded an apparent density of 70%. The majority of its cells remained open for the complete loading cycle. The 50% dense foam, which was compressed to 35%
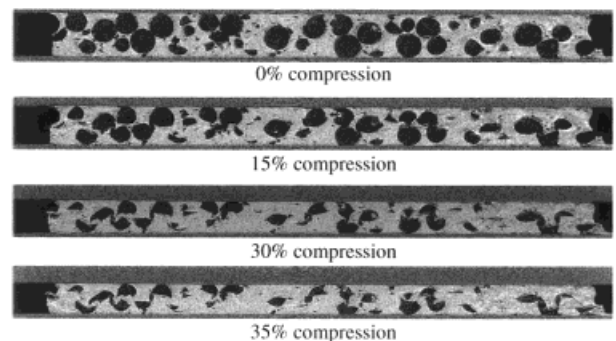

Figure 5 A through–thickness section of the foam in Figure 3 during compressive loading through 35% strain.
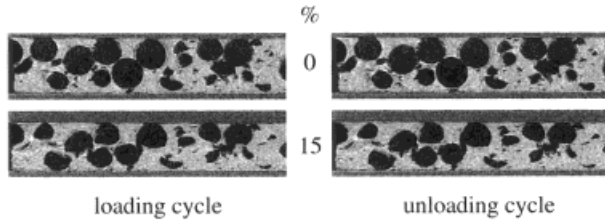
Figure 6 An expanded view of the foams during compression and recovery. Only the first and next to last stages of the strain cycle are shown. Comparison of the left (before strain) and right (during recovery) images demonstrate that registration of the foam specimens was maintained during the cycle. There was no evidence of any long-term creep or relaxation.

engineering strain, reached an apparent density of 76%. Like the lower density foam, most of its cells remained open to a 70% apparent density. However, between 70 and 75% density, the number of open cells dropped rapidly to near zero; all save the cells at the periphery became sealed-off from the surface. This behavior suggested the existence of a critical density for pore closure, ρ_c, near 75% apparent density.

The connectivity of the elastomer was measured before and after a full cycle of load and recovery. The 40% dense foam, which was compressed below the critical density, had less than a 1% change in connectivity before and after loading. The 50%

dense foam, which was compressed beyond the critical density, had a 15% increase in connectivity. This latter increase was significant and indicated that the deformation was not fully recoverable. A scan through the before and after images showed that cell wall rupture, which had occurred during the test cycle, was responsible for the increase in connectivity. Before and after images of a tomographic section through the 50% dense foam is shown in Figures 8(a,b). These before and after images demonstrate that some cell wall rupture had occurred during compression. The development and growth of tears were also observed. The tears appeared confined to regions of low contrast in the images. Because the tomogram is sensitive to material density and mean atomic number, these low-contrast areas reflect either regions where the fumed silica filler was not evenly dispersed or regions where there was preexisting porosity smaller than the spatial resolution of the imaging system. In either case, the lower image contrast implied a zone of weakness in the material.

The quasi-static elastic modulus of the 50% foam, as determined by the finite-element method at each stage of compression, is compared with the derivative of the stress–strain curve in Figure 9. When the correct value of the Poisson's ratio was used in the calculations, the finite-element results paralleled that of the experimental load-
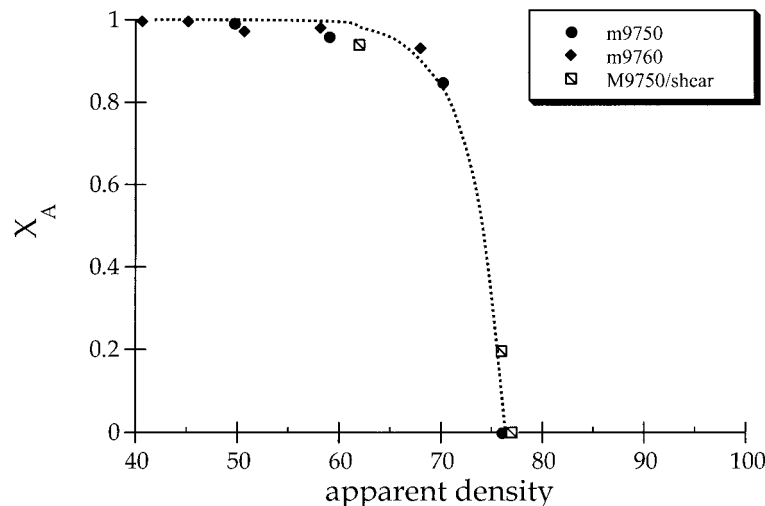

Figure 7 Fraction of open (surface connected) pores as a function of the apparent foam density during compressive loading. Between an apparent density of 70–75 %, the number of open pores decreases to zero and the foam becomes closed-cell. The abruptness of this transition is typical of critical scaling behavior. One specimen, M9750/shear, was loaded in combined compression and shear to provide an apparent density just above 75%.
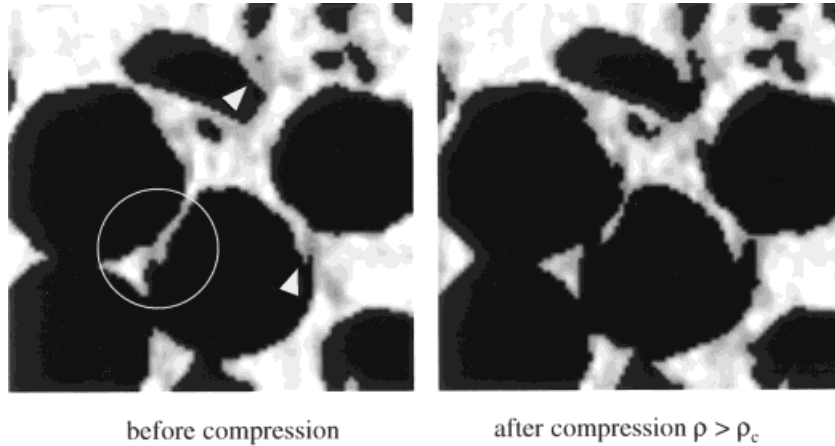
before compression

after compression $\rho > \rho_c$

Figure 8   Before and after compression images of a section of the foam showing regions where cell wall rupture had occurred (circle). The arrows point to low-contrast regions where tearing was noticed after compression. The low-contrast regions are believed to represent regions of material weakness.

ing curve, including the rapid rise near densification. When a much lower value of the Poisson ratio was used, the calculated values failed to reflect the rapid rise in stiffness at densification.

The derivatives of the theoretical models of Ben-Dor et al. and Dienes and Solem were also compared with the experimental results in Figure 9. The Dienes and Solem model agreed better with the experimental data than did the model proposed by Ben-Dor et al. However, neither approach correctly modeled the abruptness of the transition from buckling to densification.

DISCUSSION

This work demonstrated that large deformation in cellular materials can be imaged noninvasively
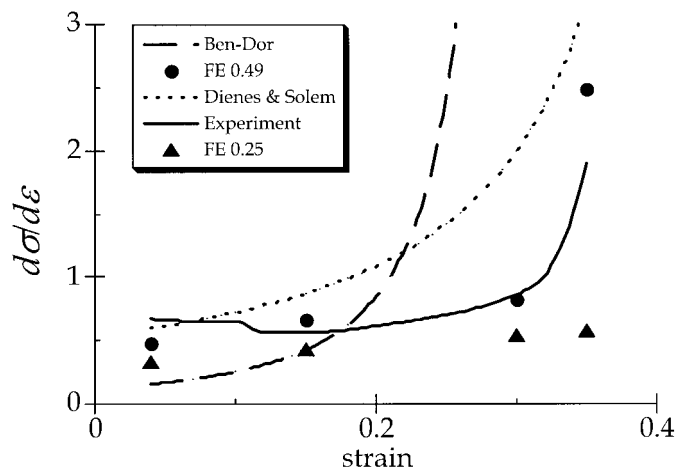

Figure 9   Comparison of (dashed lines) theory, (filled circles) finite-element modeling, and (solid line) experiment for a 50% initial density foam during compressive loading. Finite-element modeling with the correct value of the Poisson ratio (0.49) closely followed the experimental data for the entire range of compression. When a low value of the Poisson ratio was used (0.25), the finite-element model did not predict the rapid rise in stiffness near densification. Theoretical models, on the other hand, overestimated the stiffness of the foam near densification by not correctly modeling the abruptness of the transition from elastic buckling to densification.

and that the images can be used as meshes for physically based finite-element modeling. Success required integration of a load frame with a microtomography scanner. Two approaches to load a frame design for tomographic imaging were previously proposed.[17,18] The first approach, described by Breunig et al.,[17] used a radiolucent standoff to transfer load from an actuator to the specimen. With this configuration, the entire frame rotated while the standoff remained continuously in the path of the X-ray beam.

The second approach,[18] the one adopted here, used rotating load platens and held the frame stationary. This design prevented any material other than the specimen to intersect the X-ray beam. The use of a micrometer to dial-in fixed strains and the use of precision bearings to allow free rotation were the innovations in the present stage design. This design removed mechanical noise that might have been present if a mechanical actuator had been used to maintain a constant displacement. The small loads required to deform the elastomer foam (less than 1 MPa) made this approach feasible.

Open pores, which connect to the atmosphere, maintain a constant pressure balance during compression. Therefore, open porosity does not contribute to the pressure dependence of the modulus. Blind pores, on the other hand, cannot breathe; therefore, the trapped gas in blind pores contributes to the mechanical properties via the pressure-dependent terms in eqs. (1) and (2). In our present study, we found that the silicone foams remained open until a critical density between 70 and 75% was reached. At this point in the compression, the foam became a closed cell, and some contribution from gas pressure in the cell interiors could be expected. However, because the critical density occurred near full densification, this contribution would have been small.

The finite-element method, based on the physical architecture of the compressed foam, provided elastic moduli that were in good agreement with the derivative of the experimental stress–strain curve. The treatment of Ben-Dor et al., largely because it relied on model-specific values of Σ_d and $\varepsilon_{\mathrm{el}}$ and a somewhat heuristic definition of ε_D, provided the poorest fit to experiment. Inconsistencies in any of these idealized parameters would lead to large errors in the stress–strain behavior near ε_D.

The *ab initio* treatment by Dienes and Solem, on the other hand, provided a much better fit since it relied on known properties of the base elastomer. In addition, Dienes and Solem considered the specific case of foam with spherical porosity, identical to the one characterized in this study. Although the Dienes and Solem model was consistent with the general behavior of the elastomeric foam, it overestimated the material stiffness at the nascent stages of densification: a natural consequence of the hyperbolic nature of their Taylor-series expansion. In both the experimental data and the finite-element results, the transition to densification was more abrupt, occurring soon after the critical density had been reached. This latter point might be important; it suggests the possibility of critical scaling and universality, which might provide another avenue to defining the stress–strain behavior near ε_D.

From the limited experimental data presented thus far, it would be highly speculative to suggest that compressive deformation leads to critical scaling and that critical scaling might be important for describing stress–strain behavior in the vicinity of ε_D. Nevertheless, there is a physical argument that can be introduced that makes such a suggestion plausible. The sequential compression of a unit cell is shown in Figure 10. Circular openings connect the neighboring pores. As shown in Figure 10, the smaller openings were first to close with compression, followed by progressively larger openings until all pores became closed off at ρ_c. If the circular openings initially had a uniform size distribution but were randomly distributed in space, compression would have the appearance of random bond breaking. Random bond breaking leads naturally to critical scaling.[19]

The critical density marks a transition from cell wall buckling and folding to direct compression of the bulk elastomer. Since this transition occurs abruptly, the stress–strain behavior also changes abruptly above ρ_c. The model of Dienes and Solem was based on the principle of superposition of noninteracting spheres. Actually, the critical density signifies a phase transition in the pore morphology; in transitioning across ρ_c, the correlation length goes from finite to infinite. The superposition principle breaks down with discontinuous changes in length scale, and a renormalization approach might be considered instead.

Elastomeric foam is expected to exhibit full recovery from loading within the elastic regime. Deviations from full recovery result from damage such as cell wall rupture or from focal contact adhesions. In topological terms, compressive or tensile loading in the elastic regime is homeomorphic (simple
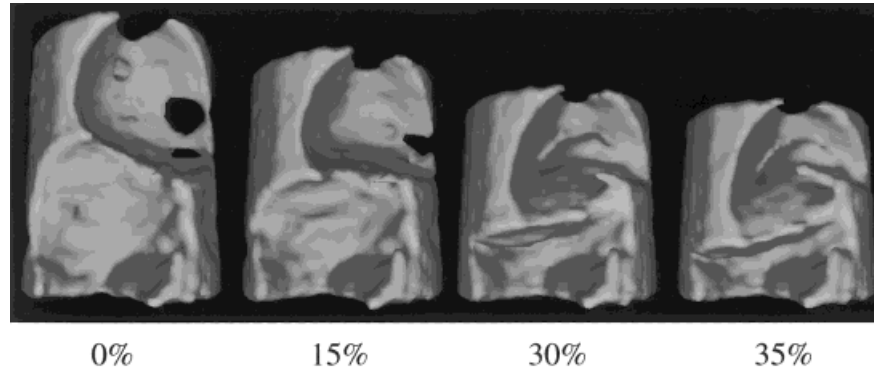
Figure 10 A sequence of three-dimensional images of the 1-mm-diameter core during compression. In these images, the smallest of the circular openings are the first to close-off during loading. Toward densification, even the largest pore openings have begun to seal off. If the size distribution of the circular pore openings is spatially random, then this pore closure process will appear like random bond breaking and lead naturally to critical scaling behavior.

stretching). In three dimensions, three parameters are invariant with respect to a homeomorphic transformation. These invariants were used to develop a rapid method for assessing whether damage occurred during the compression cycle. In the foam that was compressed beyond ρ_c, there was a significant increase in the connectivity, which should have been preserved in an undamaged specimen. Further screening showed that the increase in connectivity resulted from cell wall rupture.

There were several limitations with the present work. As this study was intended to be exploratory, only a limited number of specimens were imaged. Also, the possibility of critical scaling was not anticipated; only a few values of compressive strain were characterized. These issues will be addressed in future work. Finally, this study relied on synchrotron radiation. Although the beam time required for the work described in this article was less than 1 day, it is recognized that many researchers do not have access to a synchrotron radiation source. However, for applications that do not require high spatial resolution, tomography systems based on laboratory X-ray generators can be used instead.

CONCLUSIONS

It is possible to image the deformation behavior of cellular solids in three dimensions during loading. A simple loading device that maintained specimen registration at the micrometer scale while allowing specimen rotation in an X-ray beam was presented. The ability to use the three-dimensional images for finite-element studies was demonstrated; finite-element solutions of the elastic properties were in excellent agreement with the experimental data. Finally, the topological properties of the foam were determined and were used to rapidly assess whether unrecoverable damage had occurred during loading. It was found that foams loaded beyond a critical density for pore percolation exhibited cell wall rupture and that these ruptures were associated with pre-existing areas of weakness in the elastomer.

REFERENCES

1. Gibson, L. J.; Ashby, M. F. Cellular Solids, Structure and Properties, 2nd ed.; Pergamon Press: New York, 1997.
2. Hilyard, N. C.; Cunningham, A. Low Density Cellular Plastics, Physical Basis of Behaviour; Chapman and Hall: London, UK, 1994.
3. Warren, W. E.; Kraynik, A. M. J Appl Mech 1988, 55, 341.
4. Christensen, R. M. Zeit Angew Math Phys 1995, 46, S506.
5. Gibson, L. J.; Ashby, M. F. Proc R Soc Lond A 982, 382, 43.
6. Ben-Dor, G.; Cederbaum, G.; Mazor, G.; Igra, O. J Mater Sci 1996, 31, 1107.
7. Dienes, J. K.; Solem, J. C. Acta Mech 1999, 138, 155.

8. Kinney, J. H.; Nichols, M. C. Annu Rev Mater Sci 1992, 22, 121.

9. Weibel, E. R. Stereological Methods; Academic: New York, 1989; Vol. 2.

10. Hoshen, J.; Kopelman, R. Phys Rev B 1976, 15, 3438.

11. Feldkamp, L. A.; Goldstein, S. A.; Parfitt, A. B.; Jesion, G.; Kleerekoper, M. J Bone Miner Res 1989, 4, 3.

12. Kinney, J. H.; Haupt, D. L. J Mater Res 1997, 12, 610.

13. Ladd, A .J. C.; Kinney, J. H. Physica A 1997, 240, 349.

14. Ladd, A. J. C.; Kinney, J. H.; Haupt, D. L.; Goldstein, S. A. J Ortho Res 1998, 16, 622.

15. Ulrich, D.; Van Rietbergen, B.; Weinans, H.; Rueg-segger, P. J Biomech 1998, 31, 1187.

16. Niebur, G. L.; Yuen, J. C.; Hsia, A. C.; Keaveny, T. M. J Biomech Eng 1999, 121, 629.

17. Breunig, T. M.; Stock, S. R.; Brown, R. C. Mat Eval 1993, 51, 596.

18. Hirano, T.; Usami, K.; Tanaka, Y.; Masuda, C. J Mater Res 1995, 10, 381.

19. Stauffer, D.; Aharony, A. Introduction to Percolation Theory, 2nd ed.; Taylor and Francis: New York, 1994.